Integrating computational and experimental thermodynamics of refractory materials at high temperature

Qi-Jun Hong,^{1,*} Axel van de Walle,² Sergey V. Ushakov,³ and Alexandra Navrotsky^{1,3}

¹School for Engineering of Transport, Energy and Matter,

Arizona State University, Tempe, AZ 85287, USA

²School for Engineering, BrownUniversity, Tempe, RI 02912, USA

³School of Molecular Science, Arizona State University, Tempe, AZ 85287, USA

(Dated: October 31, 2022)

We develop new computational and experimental methods to determine materials properties at high temperature, such as melting temperature, heat of fusion, heat capacity, and lattice constant. From density functional theory, we construct the small-size coexistence method and the SLUSCHI package to compute the properties accurately, as well as to fully automate the computation process. From experiment, we build experimental approaches, including ultra-high-temperature Drop-n-Catch (DnC) calorimetry and synchrotron X-ray diffraction on solid laser-heated aerodynamically levitated samples. Employing deep learning techniques, we build an ensemble graph-neural-networks model that predicts materials properties in milliseconds. The simultaneous development of computational and experimental approaches allows us to integrate these methods and the data generated by them.

Keywords: density functional theory, machine learning, experiment, melting

High temperature materials properties, such as melting temperature, heat of fusion, and heat capacity, are very challenging to compute or measure¹, thus impeding the design and discovery of refractory materials and high temperature materials research. The chief reason for the meager data on the structure and thermodynamics of refractory materials above 2000 °C is the lack of well-established tools and methods for measurements and the complexity of ab initio calculations at these temperatures. For experiment, measuring materials properties at high temperature is often hindered by issues such as temperature gradient, sample contamination, and sample containment challenge. For computation, in particular density functional theory² (DFT) calculations, these high temperature properties are evidently different from static calculations at absolute zero, as high temperature properties often require an extensive sampling of configurational space and hence expensive DFT molecular dynamics $(MD)^{3-8}$.

Our goal is to establish the accuracy and limitations of our new experimental and computational approaches. The experimental approaches include ultrahigh-temperature Drop-n-Catch (DnC) calorimetry and synchrotron X-ray diffraction on solid laser-heated aerodynamically levitated samples. The new computational approaches include molecular dynamics methods to efficiently obtain high temperature thermodynamic properties, such as melting points and absolute free energies in the presence of large deviations from harmonic behavior, as well as their implementation as automated software tools. Given the large amounts of time and resources associated with current experimental and computational methods, we also seek to develop machine learning

approaches that are more amenable to high-throughput exploration or screening.

I. Deep learning and integration

A. Deep learning

From both experimental and computational data, we build deep learning models $^{9-11}$, aiming to predict material properties, such as melting temperature. More specifically, we seek a mapping to materials properties from the chemical formula only. No other materials or structural features are required. Once this mapping is determined, it allows us to predict melting temperature for any chemical formula without further additional input from any experiment or computation. In our view, relying on input features would reduce the broad applicability of the method, especially in high-throughput exploration or screening applications, where chemistry is typically the only a priori known input.

We first build a melting temperature database that contains mostly experimental melting temperatures, as well as DFT values based on *SLUSCHI* calculations (See Section II). This training database currently has approximately 9400 entries, while each entry is the chemical compositions, i.e., elements and their concentrations, or equivalently chemical formula, and the corresponding melting temperature. We then build a deep learning model with graph neural networks¹² (GNN) and residual neural networks¹³ (ResNet). GNN allows us to encode and incorporate the physics of the elements and chemical formula into the neural network connections. The communication among the GNN nodes is capable of detecting binary, ternary, and higher-order interactions among the elements. Our unique design of the GNN also imposes the so-called permutation invariance of chemical formula (e.g., ZrO₂ and O₂Zr are the same material), which

^{*} e-mail: qijun.hong@asu.edu

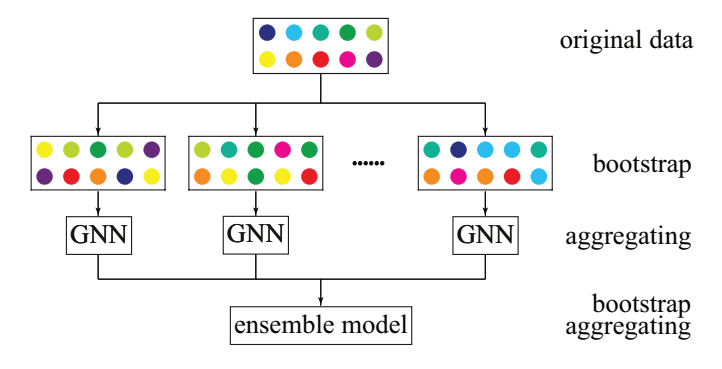


FIG. 1. The ensemble model of 30 GNN models is based on bootstrap aggregating. The benefits include (1) further overfitting reduction, (2) uncertainty estimate, and (3) outlier detection. Therefore the model facilitates integration of the experiment and computation.

TABLE I. Outlier data points detected by the ensemble model

Materials ^a	$\mathrm{MT}^b \ [\mathrm{K}]$	Correction
100% Fe + 0% C	4099	Composition: 100%C
0%Fe + $100%$ C	1809	Composition: 100%Fe
$H_2O_3 \cdot Mo_2O_3$	2053	Material: $Ho_2O_3 \cdot Mo_2O_3$
$CdFe_2O_4$	181.3	Melting point: 1813 K

 $[^]a$ Data outliers from ASM database and ChemNet. These data points are inaccurate, with wrong composition, chemical formula, or melting temperature. We review these issues and manually correct them. b MT = melting temperature.

reduces training complexity and improves efficiency by n! times, where n is the number of elements in a compound. The ResNet effectively handles the issue of diminishing gradient in model training, thus allowing deep neural networks and complex non-linear mappings. We prevent overfitting by heavily employing dropout layers in the GNN model.

The deep learning model gives us predictive capability for melting temperatures, with a root-mean-square error (RMSE) of 160K and an R^2 score of 0.933, for a hold-out test set. Furthermore, the model is extremely fast, at a speed of milliseconds per material. In Ref. 10, we have utilized the model to explore the entire chemical space and search for high-melting-point materials. We also employed the model to rapidly calculate melting temperatures on thousands of complex minerals, which led to the exciting discovery of clear trends in the melting points of minerals arising from different periods of the earth's geological history. $^{10,14-16}$.

B. Ensemble and integration

We have been improving the models by adding more data points, from both computation and experiment, into the databases. During the process, we face various challenges, particularly the inconsistency between experimental and computational data, such as data quality issues, data outliers, and systematic mismatch between experiment and computation.

To resolve these issues, we require a system that is able to estimate error and uncertainty. A large uncertainty at a certain chemical composition suggests that the current database, upon which the model is built, fails to converge to a precise value, and thus more data points are needed in the vicinity. A large error (i.e., an outlier) generally indicates two possible causes: Either (1) the data point is wrong due to data issues (so we should correct or simply remove the data point), or (2) the data point is correct and thus crucial to the mapping (so more sampling is needed to describe the function in the vicinity accurately).

We design a system that reshuffles the database to achieve these goals. By employing bootstrap aggregating (bagging)¹⁷, we build an ensemble model, aggregating a collection of 30 GNN models, as shown in Figure 1. Compared to the original GNN model, the ensemble model has three distinct benefits. First, the ensemble model is capable of estimating uncertainty of the computation, in addition to melting temperature. For each chemical formula, the 30 separate GNN models independently generate 30 different melting temperature values, from which we compute the mean and standard error. Second, the ensemble model further guards against overfitting. As bootstrap reshuffles the dataset, it generates random data populations for training, and these individual GNN models are later aggregated to the ensemble model, outperforming a single learner. Thanks to bootstrap and reshuffling, the excellent performance of the ensemble model ($R^2 = 0.99$ and 0.98, RMSE=60 and 100 K for in-the-bag and out-of-bag sets, respectively) directly proves our control of overfitting in our model. Third, the ensemble model is capable of detecting outliers, as each data point will fall in the testing sets for a portion of the 30 random bootstraps, thus allowing us to evaluate its out-of-bag error and detect outliers, i.e., data points that are far away from the trend of others. Indeed, we have found several outliers with data issues, though the number is minimal (fewer than 5 out of more than 9,000), as shown in Table I. The correction of outliers significantly improves the model's performance, as these outliers were the major contributors to errors previously, accounting for a significant portion of the RMSE.

All models are already deployed online and publicly available 18 .

C. Application: materials design and discovery

We have already completed the models for melting temperature 9,10 and bulk modulus. Employing these two models, we explore all ternary chemical space (for any chemical formula of any ternary compound) and search for high-melting-point materials, which leads to

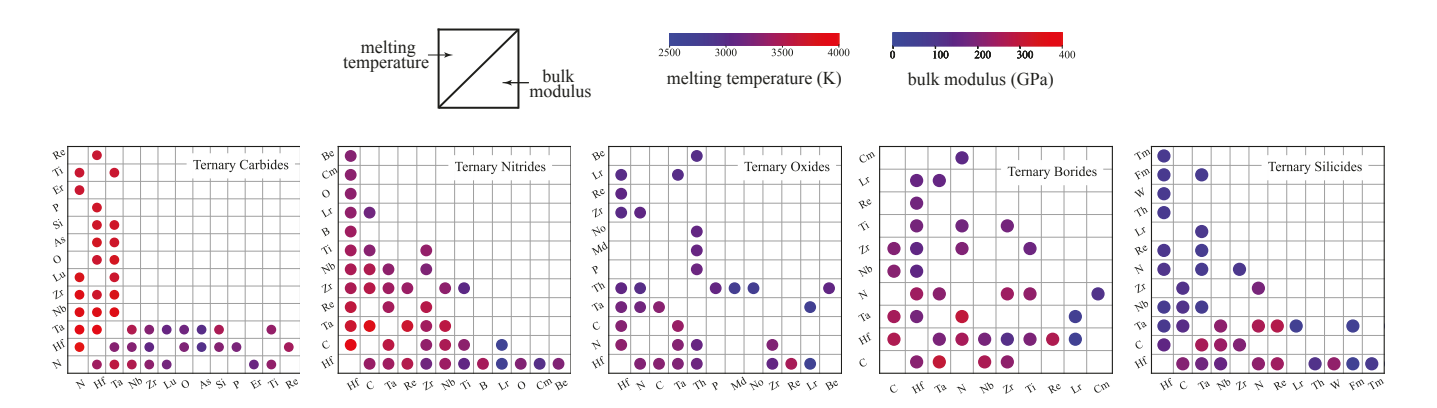


FIG. 2. Materials design and discovery of approximately 100 ternary carbides, nitrides, oxides, borides, and silicides, based on simulated annealing Monte Carlo simulations and the deep learning models of melting temperature and bulk modulus. Each dot represents a top candidate of high-melting-point material, with its melting temperature and bulk modulus predicted by the models. Each dot is a ternary compound, with two elements marked on the two axes, while the third element is determined by the figure caption, i.e., carbides, nitrides, oxides, borides, or silicides.

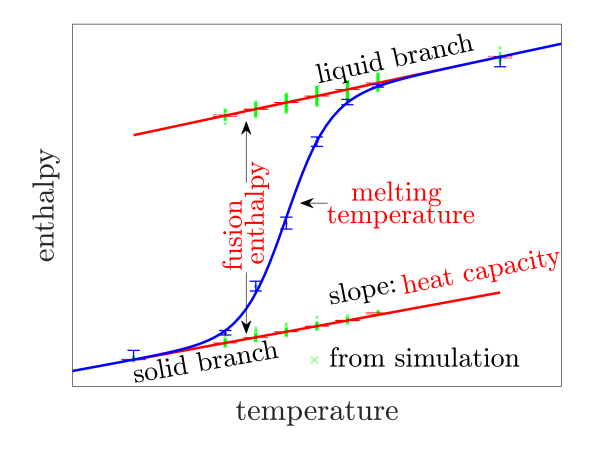


FIG. 3. DFT computation of melting temperature, heat of fusion, and heat capacity, based on the small-size coexistence method and the SLUSCHI package.

the discovery of approximately 100 ternary carbides, nitrides, oxides, borides, and silicides, as summarized in Figure 2. These computational materials discoveries will guide us in the synthesis and experimental validation of the materials.

II. DFT calculation

In addition to ML-based approaches to the exploration of high-temperature thermodynamic properties, we also utilize more targeted methods to characterize specific materials. These methods also provide very valuable input to our ML framework for chemistries where few data are available.

DFT melting temperature calculations are considered extremely expensive. We have built a method, called the small-size coexistence method, to accurately calculate melting temperature directly from DFT. Along with melting temperature are other materials properties also available after the calculation, including fusion enthalpy,

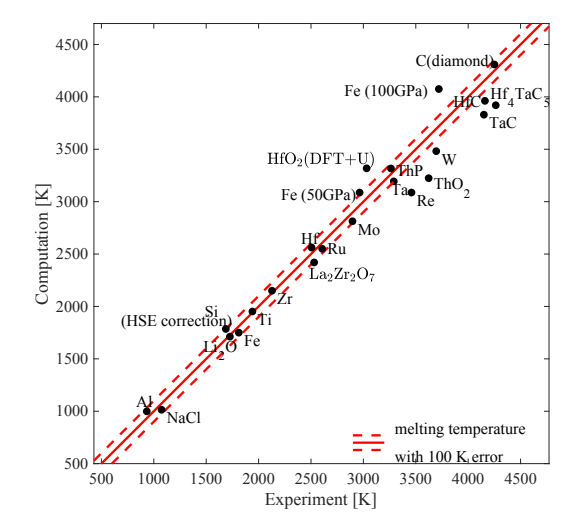


FIG. 4. Computational melting temperature based on DFT versus experiment. Error bars of 100 K were plotted as red dash lines for eye guide. Plotted are materials at ambient pressure (unless marked) that meet the requirements that (1) we have studied the materials using the method and that (2) there are existing experimental values to compare with. The GGA-PBE functional is employed unless elaborated in the label. PBE tends to underestimate melting temperature, most likely due to its under-binding nature. On the other hand, PBE-HSE often provides lower and upper boundaries of the melting temperature.

fusion entropy, and heat capacity, as illustrated in Figure 3. The method^{1,19} is highly accurate and efficient. As shown in Figure 4, the error is generally under 100K, reaching the limit of DFT functional accuracy. In terms of cost, it usually takes several days to compute one material, with a typical total cost of several thousand to tens of thousand CPU hours. Given the prohibitively high cost of other approaches (such as the

large-size coexistence method⁴ and the particle insertion method^{8,20}), the method is one of the fastest for DFT melting temperature calculation.

This DFT formalism features small-size solid-liquid coexistence MD simulations, with the melting temperature inferred from statistical analysis of the time evolution in the solid-liquid phase fractions. It eliminates the risk of metastable superheated solids in the fast-heating method 6,21 , while significantly reducing the computational cost relative to the traditional large-scale coexistence method 3 . We have utilized this method to study hundreds of materials $^{22-30}$, all based on direct DFT 2,31 MD simulations via the VASP package 32 .

We have automated the computational process into the *SLUSCHI* (Solid and Liquid in Ultra Small Coexistence with Hovering Interfaces) package³³, which we freely distribute and is publicly available on our group's website.

III. Experiment

Our experimental efforts to characterize the hightemperature thermodynamic properties of refractory materials include ultra-high-temperature Drop-n-Catch (DnC) calorimetry and synchrotron X-ray diffraction on solid laser heated aerodynamically levitated samples. Splat quenching techniques provide the highest possible cooling rates and were originally developed for quenching liquid alloys into metallic glasses. The splat quenching of five component ("high-entropy") rare earth oxide melts was tested using splittable nozzle aerodynamic levitator.³⁶ Drop-n-catch (DnC) calorimeter³⁷(Fig. 5) relies on heating with CO₂ laser and aerodynamic levitation and provides previously not realized measurements of fusion enthalpies of refractory oxide compositions^{25,26,29,38}. The main limitations of the current DnC approach are in the thermal gradient in the samples and propensity for transition into an ablation regime since the levitating bead is surface heated from the top with laser but cooled from the bottom with gas flow required for aerodynamic levitation. The necessity of flowing gas to maintain levitation also complicates the design for operation at higher pressures to reduce evaporation. Refractory carbides, borides, and nitrides of transition metals, including predicted hafnium carbonitride composition, are metallic conductors. This enables bulk heating of these compositions by electric current to reduce thermal gradient. It also provides a way for levitation without sample cooling in a gas stream. Electromagnetic levitation (EML) provides both bulk induction heating and levitation, which can be realized from vacuum to hyperbaric conditions. The feasibility of electromagnetic levitation for electrically conductive ceramics was demonstrated. It has profound implications for the collection of thermophysical data³⁹ for ultrahigh temperature ceramics and was proposed as sample environment for neutron diffraction beamline⁴⁰. This will provide benchmarking of computational data for refractory carbides, borides, and nitrides, which are under investigation as components of ultra-high temperature

ceramics and nuclear fuels.

Most of the rare earth ceramic formulations include zirconia and hafnia. Their melting temperatures are well constrained: 2710 and 2800 °C, respectively; however, their fusion enthalpies have never been measured. The multiple thermodynamic assessments of phase diagrams with ZrO₂ relied on the value from the JANAF thermochemical tables, which can be traced to estimation from liquidus slopes in an early phase diagram.²⁶ The estimation for HfO₂ fusion enthalpy relied on the same estimate and assumption of the same entropy of fusion. There were no data on volume change on tetragonal to cubic phase transformation and on thermal expansion of cubic zirconia and hafnia phases. Thus, after the construction and validation of the new drop-and-catch calorimeter, ZrO₂ and HfO₂ were chosen for joint computational and experimental investigation, including measurements of fusion enthalpies of in situ high temperature synchrotron diffraction experiments on solids at APS. Both methods employ aerodynamic levitation with laser heating, which is still under active development.

The agreement in fusion enthalpies from experiment and computation was remarkable, e.g., $55 \pm 7 \text{ kJ/mol}$ vs. 54 ± 2 kJ/mol, respectively, for ZrO₂. We also observed good correspondence in thermal expansion of cubic ZrO₂ from XRD and DFT MD modeling. These results validate the reliability of high temperature heat capacity data obtained exclusively from computations, which are critical for thermodynamic modeling but are not currently accessible by experimental means. On the other hand, the value for fusion enthalpy of ZrO₂ from our measurements and computations is significantly lower than the estimated value (87 kJ/mol) included in JANAF table of thermochemical data. The reason is that we include the dynamic disorder on oxygen sublattice in high temperature cubic ZrO₂ and HfO₂ in both our experiment and computation, while the JANAF values are obtained via extrapolation of early phase diagrams and do not include disordering effects, which is evident from our high temperature diffraction data and computed structure, heat capacities, and oxygen diffusion coefficients. This joint work demonstrated the capabilities of the new integrated computational and experimental approaches in providing a full set of high temperature thermodynamic properties.²⁶ We employed the same strategy of combined experimental-computational investigation²⁹ of high temperature structure and thermodynamics to two of the most refractory rare earth oxides: Lu₂O₃ and Yb₂O₃ with melting temperatures of 2490 and 2435 °C, respectively. We also demonstrated good agreement between experiment and computation on the negative volume change on high temperature cubic to hexagonal transformation in Er₂O₃, Ho₂O₃, and Tm₂O₃. As shown in Figure 6, the computational results are now being correlated with experimental data to yield a combined set of high temperature thermodynamic properties for RE₂O₃ phases, including thermal expansion, which is needed for the 3rd generation Calphad database.

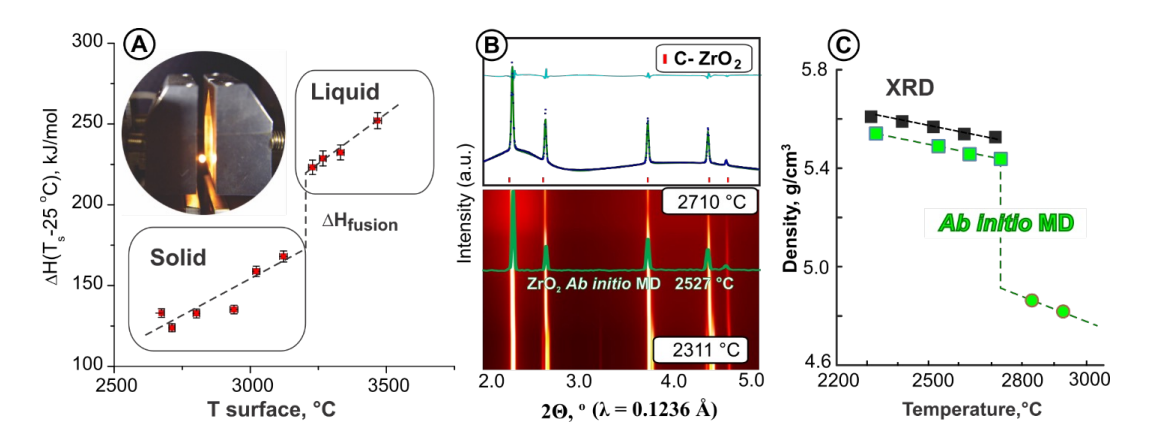


FIG. 5. Combined computational and experimental investigation of ZrO₂ above 2000 °C. (A) Experimental measurement of fusion enthalpy by drop-and-catch calorimetry. (B) High temperature synchrotron X-ray diffraction experiments to the melting temperature, (C) Density of cubic and liquid ZrO₂ from experiment and computations.²⁶

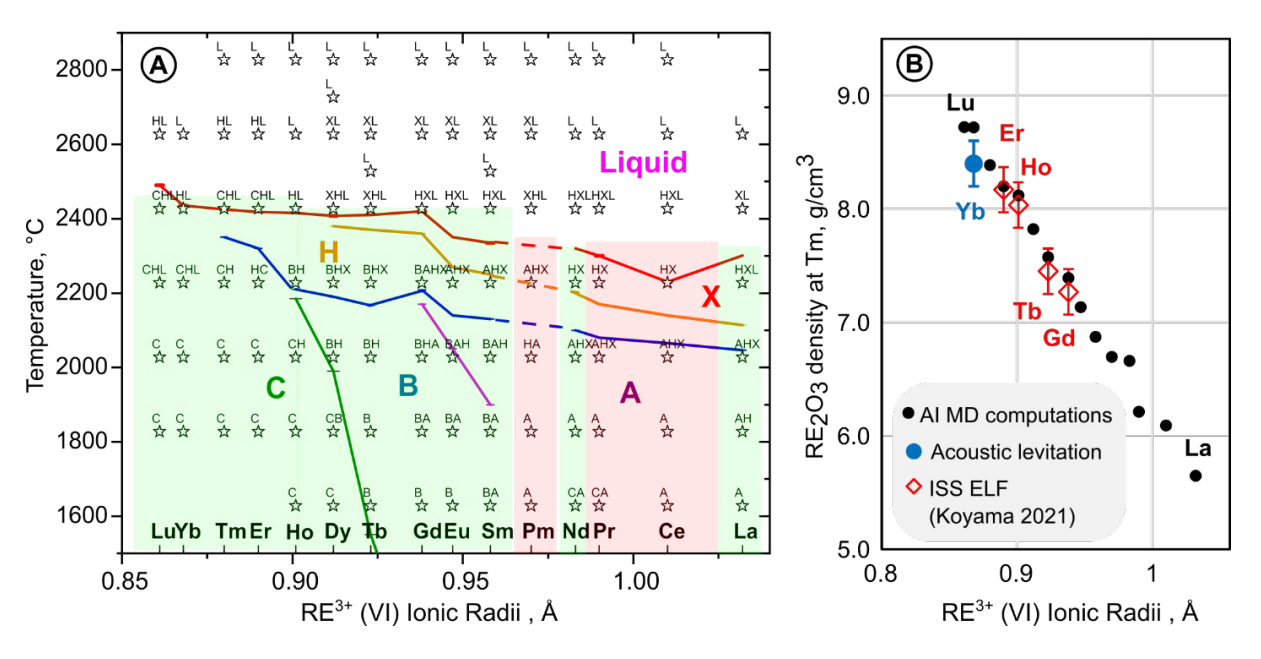


FIG. 6. (A) Current computational matrix for C, B, H, X, and liquid phases in rare earth sesquioxides (total 7.7×10^6 CPU/hours). Green highlights indicate where new structural and thermodynamic properties are acquired for validation. (B) Volume change on melting of RE₂O₃ from computations compared with experimental data. 34,35

IV. Summary

We have built new computational and experimental methods to determine material properties at high temperatures. From DFT calculations, we built the small-size coexistence method to compute melting temperature, fusion enthalpy and entropy, and heat capacity. From experiment, we built ultra-high-temperature Drop-n-Catch (DnC) calorimetry and synchrotron X-ray diffraction on solid laser heated aerodynamically levitated samples to measure fusion enthalpy, melting temperature, and crystal structure. From deep learning, we have built databases and models to predict melting temperature and heat capacity. We utilize bootstrap aggregating to build an ensemble model, which enables

us to integrate data points from these computational and experimental methods.

Acknowledgements

This research was funded by the U.S. National Science Foundation under Collaborative Research Awards DMR-2015852, 2209026 (ASU) and DMR-1835939, 2209027 (Brown University) with use of Research Computing at Arizona State University and the Extreme Science and Engineering Discovery Environment (XSEDE), supported by National Science Foundation Grant No. ACI-1548562. Hong would like to thank Qiang Zhu for discussion.

Data Availability

The raw/processed DFT data required to reproduce these findings are available to download from https://faculty.engineering.asu.edu/hong/systems-

tested/. The machine learning data are available at https://faculty.engineering.asu.edu/hong/melting-temperature-predictor/. The experimental data will be made available on request.

- Q.-J. Hong, Methods for Melting Temperature Calculation, Ph.D. thesis, California Institute of Technonology (2015).
- ² P. Hohenberg and W. Kohn, Phys. Rev. **136**, B864 (1964).
- ³ O. Sugino and R. Car, Physical Review Letters 74, 1823 (1995).
- ⁴ J. R. Morris, C. Z. Wang, K. M. Ho, and C. T. Chan, Physical Review B 49, 3109 (1994).
- J. Mei and J. W. Davenport, Physical Review B 46, 21 (1992).
- ⁶ A. B. Belonoshko, N. V. Skorodumova, A. Rosengren, and B. Johansson, Physical Review B - Condensed Matter and Materials Physics **73**, 1 (2006).
- ⁷ S. T. Lin, M. Blanco, and W. A. Goddard, Journal of Chemical Physics 119, 11792 (2003).
- ⁸ B. Widom, Journal of Physical Chemistry **86**, 869 (1982).
- ⁹ Q.-J. Hong, arXiv (2021), 10.48550/ARXIV.2110.10748.
- ¹⁰ Q.-J. Hong, S. V. Ushakov, A. van de Walle, and A. Navrotsky, Proceedings of the National Academy of Sciences, In Press (2022).
- ¹¹ Q.-J. Hong, Computational Materials Science **214**, 111684 (2022).
- ¹² F. Scarselli, M. Gori, A. C. Tsoi, M. Hagenbuchner, and G. Monfardini, IEEE Transactions on Neural Networks 20, 61 (2009).
- ¹³ K. He, X. Zhang, S. Ren, and J. Sun, 2016 IEEE Conference on Computer Vision and Pattern Recognition (CVPR), 770 (2016).
- ¹⁴ R. M. Hazen, D. Papineau, W. Bleeker, R. T. Downs, J. M. Ferry, T. J. McCoy, D. A. Sverjensky, and H. Yang, American Mineralogist 93, 1693 (2008).
- ¹⁵ S. V. Krivovichev, V. G. Krivovichev, and R. M. Hazen, European Journal of Mineralogy 30, 231 (2018).
- ¹⁶ S. M. Morrison and R. M. Hazen, American Mineralogist 105, 1508 (2020).
- ¹⁷ L. Breiman, Machine Learning **24**, 123 (1996).
- ¹⁸ "Melting temperature predictor based on machine learning," https://faculty.engineering.asu.edu/hong/melting-temperature-predictor/, accessed: 2022-08-14.
- ¹⁹ Q.-J. Hong and A. van de Walle, Journal of Chemical Physics **139**, 094114 (2013).
- ²⁰ Q.-J. Hong and A. van de Walle, Journal of Chemical Physics 137, 094114 (2012).
- ²¹ D. Alfe, C. Cazorla, and M. J. Gillan, Journal of Chemical Physics **135** (2011), 10.1063/1.3605601.
- Q.-J. Hong and A. van de Walle, Physical Review B
 Condensed Matter and Materials Physics 92, 020104 (2015).
- ²³ Q.-J. Hong, S. Ushakov, A. Navrotsky, and A. van de Walle, Acta Materialia 84, 275 (2015).

- ²⁴ L. Miljacic, S. Demers, Q.-J. Hong, and A. van de Walle, Calphad: Computer Coupling of Phase Diagrams and Thermochemistry 51, 133 (2015).
- D. Kapush, S. Ushakov, A. Navrotsky, Q.-J. Hong, H. Liu, and A. van de Walle, Acta Materialia 124, 204 (2017).
- ²⁶ Q.-J. Hong, S. V. Ushakov, D. Kapush, C. J. Benmore, R. J. Weber, A. van de Walle, and A. Navrotsky, Scientific Reports 8, 1 (2018).
- ²⁷ Q.-J. Hong and A. van de Walle, Physical Review B **100**, 140102 (2019).
- ²⁸ S. Ushakov, A. Navrotsky, Q.-J. Hong, and A. van de Walle, Materials 12, 2728 (2019).
- ²⁹ M. Fyhrie, Q.-J. Hong, D. Kapush, S. Ushakov, H. Liu, A. van de Walle, and A. Navrotsky, Journal of Chemical Thermodynamics 132, 405 (2019).
- ³⁰ Q.-J. Hong, J. Schroers, D. Hofmann, S. Curtarolo, M. Asta, and A. van de Walle, npj Computational Materials 7, 1 (2021).
- ³¹ W. Kohn and L. J. Sham, Phys. Rev. **140**, A1133 (1965).
- ³² G. Kresse and D. Joubert, Phys. Rev. B **59**, 1758 (1999).
- ³³ Q.-J. Hong and A. van de Walle, Calphad: Computer Coupling of Phase Diagrams and Thermochemistry **52**, 88 (2016).
- ³⁴ S. V. Ushakov, J. Niessen, D. G. Quirinale, R. Prieler, A. Navrotsky, and R. Telle, Materials 14 (2021).
- ³⁵ C. Koyama, T. Ishikawa, H. Oda, H. Saruwatari, S. Ueno, M. Oshio, Y. Watanabe, and Y. Nakata, Journal of the American Ceramic Society 104, 2913 (2021).
- ³⁶ S. V. Ushakov, S. Hayun, W. Gong, and A. Navrotsky, Materials 13 (2020).
- ³⁷ S. V. Ushakov, A. Shvarev, T. Alexeev, D. Kapush, and A. Navrotsky, Journal of the American Ceramic Society 100, 754 (2017).
- ³⁸ M. Lepple, S. V. Ushakov, K. Lilova, C. A. Macauley, A. N. Fernandez, C. G. Levi, and A. Navrotsky, Journal of the European Ceramic Society 41, 1629 (2021).
- ³⁹ S. V. Ushakov, A. Navrotsky, X. Xiao, and J.Brillo (2022) in Ultra-High Temperature Ceramics: Materials For Extreme Environment Applications V, Eds by D. Butts, C. Carney, C. Tallon, G. Thompson, C. Weinberger, ECI Symposium Series.
- ⁴⁰ B. Haberl, D. G. Quirinale, C. W. Li, G. E. Granroth, H. Nojiri, M.-E. Donnelly, S. V. Ushakov, R. Boehler, and B. L. Winn, Review of Scientific Instruments 93, 083907 (2022).